Al Composition Dependence of Band Offsets for SiO_2 on α-$(Al_xGa_{1-x})_2O_3$

Xinyi Xia[1], Chaker Fares[1], Fan Ren[1], Anna Hassa[2], Holger von Wenckstern[2], Marius Grundmann[2] and S. J. Pearton[3]

[1] Department of Chemical Engineering, University of Florida, Gainesville FL 32611 USA

[2]Universität Leipzig, Felix-Bloch-Institut für Festkörperphysik, 04103 Leipzig, Germany

[3] Department of Materials Science and Engineering, University of Florida, Gainesville FL 32611 USA

Abstract

Valence band offsets were measured by X Ray Photoelectron Spectroscopy for SiO_2 deposited by Atomic Layer Deposition on α-$(Al_xGa_{1-x})_2O_3$ alloys with x= 0.26-0.74 grown with a continuous composition spread to enable investigations of the band alignment as a function of the alloy composition. From measurement of the core levels in the alloys, the bandgaps were determined to range from 5.8 eV (x=0.26) to 7eV (x=0.74). The valence band offsets were -1.2 eV for x=0.26, -0.2 eV for x=0.42, 0.2 eV for x=0.58 and 0.4 eV for x=0.74. Given the bandgap of the SiO_2 was 8.7 eV, this led to conduction band offsets of 4.1 eV (x=0.26) to 1.3 eV (x=0.74). The band alignments were nested for x>0.5, but at lower Al contents the conductions band offsets were negative, with a staggered band alignment. This shows the challenge of finding appropriate dielectrics for this ultra-wide bandgap semiconductor system.

Introduction

$(Al_xGa_{1-x})_2O_3$ is an ultra-wide bandgap semiconductor that is attracting attention for use in high power transistors and deep ultraviolet (DUV) photodetectors [1-4]. To this point, most of the work has focused on the β-polytype with a bandgap tunability ranging from 4.8 eV (Ga_2O_3) to 8.7 eV (Al_2O_3) [1,2]. The advantages of β-$(Al_xGa_{1-x})_2O_3$ grown on β-Ga_2O_3 include the high channel mobility at the interface and ability to use the heterostructure in field effect transistor structures with improved mobility, as well as Schottky diodes and photodetectors [1,2]. A drawback of this materials system during growth with techniques such as Metal Organic Chemical Vapor Deposition is the difficulty in maintain phase stability at high Al contents [1]. The α-polytype is a potential solution to extending the stability to higher Al contents and higher temperatures [2-12]. This metastable, corundum crystal structure α-polytype, transforms to the β-polymorph at temperatures above 750-900°C under equilibrium conditions [5]. Of all reported polymorphs, this phase has the highest optical bandgap with energies ranging between 5.0 eV and 5.3 eV for the binary. A number of different growth methods have recently been shown to produce high quality rhombohedral α-$Al_xGa_{1-x})_2O_3$ over a broad composition range [6-48] and in particular, the use of Al_2O_3 cap layers during annealing is able to preserve the α-phase [16]. The α-polytype has an even larger bandgap than the β-polytype and can be grown on low-cost c-plane sapphire substrates which have the same lattice structure, albeit with relatively high dislocation densities [2, 19, 22, 43]. Figure 1 shows the crystal structure of rhombohedral α-Ga_2O_3. This rhombohedral phase can also occur for Al_2O_3 and In_2O_3, which allows a potential bandgap engineering over the entire composition range [34,45,46], rendering this polymorph interesting for deep UV photodetectors or quantum-well infrared photodetectors [1,2], in addition to the power device applications [35-37].

It is clearly of interest to establish the band alignments for commonly employed dielectrics on this materials system. SiO_2 is one of the most promising choices, due to its large bandgap and maturity as a dielectric in semiconductor devices. We have previously measured the band alignment and its thermal stability for SiO_2 and Al_2O on β- $Al_xGa_{1-x})_2O_3$ for $0.2< x <0.65$ [51,52]**.** In this paper we report on the measurement of valence band offsets in the SiO_2/α-$Al_xGa_{1-x})_2O_3$ system using alloys grown by Pulsed Laser Deposition (PLD)[49,50] over a wide composition range. This was done using circular half-segmented (Ga_2O_3/Al_2O_3) ceramic targets to synthesize large diameter large thin films with a lateral varying cation composition [1,7,8,45,46]. Since the bandgap of the α-polytype alloys is even larger than those of the β-polytype alloys, this system represents a test in terms of finding dielectrics that exhibit acceptable band offsets (> 1eV is a common rule of thumb) in both the conduction and valence bands.

Experimental

The α-$Al_xGa_{1-x})_2O_3$ alloys were grown by combinatorial PLD using a KrF excimer laser (Coherent LPX Pro 305, 248 nm, 2.6 $J.cm^{-2}$) directed through a quartz window onto a segmented ceramic target (Ga_2O_3/Al_2O_3) under an O_2 partial pressure [1,49,50]. The substrate and target were mounted rotatable opposite each other at a distance of 10 cm and with a small lateral offset to each other [46]. PLD has been utilized previously to obtain AGO alloys over a broad composition range for both αand β-polytypes [8, 20, 40] The resulting cation ratio was determined by energy dispersive X-ray spectroscopy (EDX) measurements performed using a FEI Nova Nanolab 200 equipped with an Ametek EDAX detector and the crystal structure by X-ray diffraction (XRD). measured by a PANalytical X'pert PRO MRD diffractometer equipped with a PIXcel3D detector operating in 1D scanning line mode with 255 channels (for 2Θ-ω scans), receiving slit mode (for Φ-scans) and fast 2D frame based mode (for reciprocal space maps). The cation gradient ranged

between x= 0.13 and x=0.84 as measured by EDX and marked as black dots in Figure 2(a). The composition between these data points was interpolated and the resulting cation ratio represented as false color map. Along the cation gradient direction, marked with a black arrow, additional EDX measurements were performed in 1mm steps to obtain the spatial Al dependence with high lateral resolution as shown in Figure 2(b) [20]. The Al incorporation covers a range of $0.13 \leq x \leq 0.84$. The rhombohedral crystal structure of the thin films was confirmed by the 2Θ-ω XRD scans. The resulting false color map is presented in Figure 3 and reveals the crystallization in the rhombohedral phase in the entire investigated Al range. We examined four compositions, x=0.26, 0.42, 0.58 and 0.74. More details and discussion on the characterization of these samples can be found in Hassa et al. [20].

The SiO_2 layers were deposited by Atomic Layer Deposition (ALD) at 200°C using the thermal mode in a Cambridge Nano Fiji 200. The precursors were Tris (dimethylamino) silane and an inductively coupled plasma (ICP) of O_2 at 300 W [51,52]. After solvent cleaning, the substrates were exposed to Ozone for 15 min to form a protective oxide that is easily thermally desorbed during the ALD step. Both thick (200 nm) and thin (1.5 nm) layers of SiO_2 were deposited for measuring bandgaps and core levels on the α-$(Al_xGa_{1-x})_2O_3$.

XPS survey scans were performed to measure the chemical state of the SiO_2 and $(Al_xGa_{1-x})_2O_3$ layers in a Physical Instruments ULVAC PHI, with an Al x-ray source (energy 1486.6 eV, source power 300W)[51-53]. The analysis size was 100 μm diameter, with a take-off angle of 50° and acceptance angle of ±7 degrees. The electron pass energy was 23.5 eV for high-resolution scans and 93.5 eV for survey scans. The total energy resolution of this XPS system is 0.5 eV, and the accuracy of the observed binding energy is ~ 0.03 eV. Charge compensation was performed using an electron flood gun and simultaneous ion beam. The C 1*s* core levels of the surface

adsorbate (284.8 eV) were used to calibrate the binding energy [53]. Only the relative energy position is needed to determine the valence band offsets, so the absolute energy calibration has no effect on that offset. The samples were electrically insulated from the chuck to avoid uneven charge dispersion along the sample. All electron analyzers and equipment were grounded. Differential charging was not observed in any of the samples with the use of the electron gun [51,52].

The SiO_2 bandgap was obtained from Reflection Electron Energy Loss Spectroscopy (REELS) using a 1 kV electron beam and hemispherical electron analyzer. The bandgaps of the $(Al_xGa_{1-x})_2O_3$ for each composition were obtained from XPS energy loss measurements of the O1S peak. This is done simultaneously with the band alignment measurements [52,53].

Results and Discussion

Figure 4 shows the high resolution XPS spectra for the α- $(Al_xGa_{1-x})_2O_3$ to SiO_2 vacuum-core delta regions of the four compositions, while the data for the SiO_2 is shown in Figure 5. The valence band offsets were extracted from the shift of the core levels for the heterostructure samples with the thin dielectric on top of the four different compositions of the alloy. A compilation of the valence band maxima (VBM) are collected in Table 1, with values of (2.7±0.15) eV for x=0.26, (3.3±0.15) eV for x=0.42, (4.4±0.15)eV for x=0.58 and (4.5±0.15) eV for x=0.74. These were obtained by fitting of the leading edge of the valence band. The error bars in the different binding energies were combined in a root sum square relationship to determine the overall error bars in the valence band offsets (ΔE_V) [51]. These band offsets are then obtained by measuring the shift of the core levels in the α- $(Al_xGa_{1-x})_2O_3$ when SiO_2 was deposited. These are also tabulated in Table 1, with values of -1.2 eV for x=0.26, -0.2 eV for x=0.42, 0.2 eV for x=0.58 and 0.4 eV for x=0.74.

Once the valence band offsets are established, to determine the conduction band offset, it is necessary to measure the band gap of each composition. We measured the bandgaps of the four $(Al_xGa_{1-x})_2O_3$ compositions, as shown in Figure 6 (a), from the separation between the core level peak energy and the onset of inelastic (plasmon) losses in each O 1s photoemission spectra [36]. To find the band-gap energy, a linear fit is made to the measured loss spectra curve near the approximate location of onset of inelastic losses. Next, by subtracting the background, the "zero" level is determined. The energy corresponding to the onset of inelastic losses is found by extrapolating the linear-fit line and calculating its intersection with the "zero" level [33,40]. The bandgap energy is equal to the difference between the core-level peak energy and the onset of inelastic losses.

The bandgap energies were determined as 5.8 eV for x=0.26, 6.1 eV for x=0.42, 6.4 eV for x=0.58 and 7 eV for x= 0.74, respectively. Figure 7 shows the relationship between bandgap of the alloys and Al composition for our samples. As previously reported, the bandgap as a function of composition, x, is given by [28,54]

$$E_G(x) = (1-x)E_G^{GaO} + xE_G^{AlO} - bx\,(1-x)$$

where E_G^{GaO} and E_G^{AlO} are the bandgaps of the α-polytype binary endpoints and b is the bowing parameter. This has been previously reported in the range 0.84-2.13 [9, 34]. We get a value closer to 3 for our samples in the composition range measured. It was noted by Varley [53] that the *b* values are strongly influenced by the selective occupation of different cation sublattice by Al and that a single bowing parameter is not accurate over the entire composition range

The SiO_2 bandgap was obtained from Reflection Electron Energy Loss Spectroscopy (REELS) and showed a value of 8.7 eV, similar to previous reports [51,52].

The conduction band offsets ΔE_C were obtained from the relation

$$\Delta E_C = E_G^{SiO2} - E_G^{GaO} - \Delta E_V$$

The corresponding conduction band offsets were 4.1 eV (x=0.26), 2.8 eV (x=0.46), 2.1 eV (x=0.58) and 1.30 eV (x=0.74).

Figure 7 shows the band diagrams for the SiO_2/α$(Al_xGa_{1-x})_2O_3$ heterostructure. The SiO_2 has adequate conduction band offsets, but the valence band offsets are small and actually negative at x<0.5. These would be inadequate confinement of holes in SiO_2/ α- $(Al_xGa_{1-x})_2O_3$ samples over the entire composition range. The conduction band offsets are high enough to provide effective electron confinement. The SiO_2/ $(Al_xGa_{1-x})_2O_3$ band alignment is type I for x>0.5 and staggered for x<0.5. It will be interesting to measure the band alignments for Al_2O_3 deposited on the α-$(Al_xGa_{1-x})_2O_3$ alloys, since that is one of the few dielectrics with a high enough bandgap to provide effective carrier confinement for electrons and holes in these alloys.

Summary and Conclusions

The valence band offsets of SiO_2/ α-$(Al_xGa_{1-x})_2O_3$ heterojunctions were measured over a range of Al contents (x=0.26 - 0.74). The band alignments are staggered type II for x<0.5 and straddling type I for x>0.5, with conduction band offsets >1.3 eV across the composition range examined. The thermal stability of this system is of interest for future work, as the α-polytype I not the most energetically favorable state, although kinetically limited process such as rapid thermal annealing will be able to be used in device processing steps without major issues.

Acknowledgments

The work was performed as part of Interaction of Ionizing Radiation with Matter University Research Alliance (IIRM-URA*)*, sponsored by the Department of the Defense, Defense Threat Reduction Agency under award HDTRA1-20-2-0002. The content of the information does not necessarily reflect the position or the policy of the federal government, and no official

endorsement should be inferred. The work at UF was also supported by NSF DMR 1856662 (James Edgar). The authors at Leipzig thank Jörg Lenzner for EDX measurements and Monika Hahn for PLD target preparation. A.H. acknowledges support by the European Social Fund within the Young Investigator Group "Oxide Heterostructures" (SAB 100310460) and the Leipzig School for Natural Sciences BuildMoNa.

References

1. Elaheh Ahmadi and Yuichi Oshima, J. Appl. Phys. **126**, 160901 (2019).

2. H. von Wenckstern: Group-III Sesquioxides: Growth, Physical Properties and Devices, Advanced Electronic Materials, 3, 1600350 (2017).

3. T. Kawaharamura, G. T. Dang, and M. Furuta, Jpn. J. Appl. Phys. 51, 040207 (2012).

4. Y. Oshima, E.G. Víllora, and K. Shimamura, Appl. Phys. Express 8, 055501 (2015).

5. D. Machon, P. F. McMillan, B. Xu, and J. Dong, Phys. Rev. B 73, 094125 (2006).

6. D. Shinohara and S. Fujita, Jpn. J. Appl. Phys. 47, 7311 (2008).

7. A. Hassa, C. Sturm, M. Kneiß, D. Splith, H. von Wenckstern, T. Schultz, N. Koch, M. Lorenz, and M. Grundmann, APL Materials, 8, 021103 (2020).

8. A. Hassa, C. Wouters, M. Kneiß, D. Splith, C. Sturm, H. von Wenckstern, M. Albrecht, M. Lorenz, and M. Grundmann, J. Phys D: Applied Physics, 53, 485105 (2020).

9. R. Jinno, C. S. Chang, T Onuma, Y. Cho, S-Ting Ho, D. Rowe, M. C. Cao, K. Lee, V. Protasenko, D. G. Schlom, D. A. Muller, H. G. Xing, D. Jena, Sci Adv 7,eabd5891 (2021).

10. A. F. M. Anhar Uddin Bhuiyan, Zixuan Feng, Lingyu Meng and Hongping Zhao, J. Mat Res (in press, 2021).

11. M. Lorenz, S. Hohenberger, E. Rose, and M. Grundmann, Appl. Phys. Lett. 113, 231902 (2018).

12. M Hilfiker, U Kilic, M Stokey, R Jinno, Y Cho, HG Xing, D Jena, R Korlacki, Mathias Schubert, Appl. Phys. Lett. 119 (9), 092103 (2021).

13. R. Jinno, T. Uchida, K. Kaneko, and S. Fujita, Appl. Phys. Express 9, 071101 (2016).

14. S. Fujita and K. Kaneko, J. Cryst. Growth 401, 588 (2014).

15. K. Kaneko, K. Suzuki, Y. Ito, and S. Fujita, J. Cryst. Growth 436, 150 (2016).

16. J.P. McCandless, C.S. Chang, K. Nomoto, J. Casamento, V. Protasenko, P. Vogt, D. Rowe, K. Gann, S.T. Ho, W. Li, R. Jinno, Y. Cho, A.J. Green, K.D. Chabak, D.G. Schlom, M.O. Thompson, D.A. Muller, H.G. Xing and D. Jena, Appl. Phys. Lett. 119 , 062102 (2021)

17. K. Akaiwa and S. Fujita, Jpn. J. Appl. Phys. 51, 070203 (2012).

18. M. Oda, R. Tokuda, H. Kambara, T. Tanikawa, T. Sasaki, and T. Hitora, Appl. Phys. Express 9, 021101 (2016).

19. K. Akaiwa, K. Kaneko, K. Ichino, and S. Fujita, Jpn. J. Appl. Phys. 55, 1202BA (2016).

20. A. Hassa, P. Storm, M. Kneiß, D. Splith, H. von Wenckstern, M. Lorenz and M. Grundmann, Physica Status Solidi B, 2000394 (2020).

21. J. E. N. Swallow, R. G. Palgrave, P. A. E. Murgatroyd, A. Regoutz, M. Lorenz, A. Hassa, M. Grundmann, H. von Wenckstern, J. B. Varley, and T. D. Veal, ACS Appl. Mater. Interf.,13, 2807 (2021).

22. Y. Oshima, K. Kawara, T. Shinohe, T. Hitora, M. Kasu, and S. Fujita, APL Mater. 7, 022503 (2019).

23. Y. Oshima, Heteroepitaxial growth of α and ε-Ga_2O_3, in Gallium Oxide: Crystal Growth, Materials Properties, and Devices (Springer, 2019).

24. H. Sun, K.-H. Li, C. G. T. Castanedo, S. Okur, G. S. Tompa, T. Salagaj, S. Lopatin, A. Genovese, and X. Li, Cryst. Growth Des. 18, 2370 (2018).

25. B.W. Krueger, C.S. Dandeneau, E.M. Nelson, S.T. Dunham, F.S. Ohuchi, and M.A. Olmstead, J. Am. Ceram. Soc. 99, 2467 (2016).

26. Y.W. Zhang, A. Neal, Z Xia, C. Joishi, J.M. Johnson, Y. Zheng, S. Bajaj, M. Brenner, D. Dorsey, K. Chabak, G. Jessen, J. Hwang, S. Mou, J.P. Heremans and S. Rajan, Appl. Phys. Lett. 112, 173502 (2018).

27. F.B. Zhang, K. Saito, T. Tanaka, M. Nishio, M. Arita, and Q.X. Guo, Appl. Phys. Lett. 105, 162107 (2014).

28. T. Uchida, R. Jinno, S. Takemoto, K. Kaneko, and S. Fujita,.Jpn. J. Appl. Phys. 57, 040314 (2018).

29. Q. Feng, X. Li, G. Han, L. Huang, F. Li, W. Tang, J. Zhang,and Y. Haoet, Opt. Mater. Express 7, 1240 (2017).

30. C. Kranert, M. Jenderka, J. Lenzner, M. Lorenz, H. von Wenckstern, R. Schmidt-Grund, and M. Grundmann, J. Appl. Phys. 117, 125703 (2015).

31. B. Mazumder, Jith Sarker, Yuewei Zhang, Jared M. Johnson, Menglin Zhu, Siddharth Rajan and Jinwoo Hwang, Appl. Phys. Lett. 115, 132105 (2019).

32. Baishakhi Mazumdera and Jith Sarker, J. Mater. Res.36, 52 (2020).

33. S.-H. Yuan, C.-C. Wang, S.-Y. Huang, and D.-S. Wuu, IEEE Electr. Dev. Lett. 39, 220 (2018).

34. G.T. Dang, T. Yasuoka, Y. Tagashira, T. Tadokoro, W. Theiss and T. Kawaharamura:. Appl. Phys. Lett. 113, 062102 (2018).

35. E. Ahmadi, O.S. Koksaldi, X. Zheng, T. Mates, Y. Oshima, U.K. Mishra, J.S. Speck, Appl. Phys. Express 10, 071101 (2017).

36. S. Krishnamoorthy, Z. Xia, C. Joishi, Y. Zhang, J. McGlone, J. Johnson, M. Brenner, A.R. Arehart, J. Hwang, S. Lodha, and S. Rajan, Appl. Phys. Lett. 111, 023502 (2017).

37. Y. Zhang, C. Joishi, Z. Xia, M. Brenner, S. Lodha, and S. Rajan, Appl. Phys. Lett. 112, 233503 (2018).

38. J.B. Varley, A. Perron, V. Lordi, D. Wickramaratne, and J.L. Lyons, Appl. Phys. Lett. 116, 172104 (2020).

39. A.F.M. Anhar Uddin Bhuiyan, Z. Feng, J.M. Johnson, Z.Chen, H.L. Huang, J. Hwang, and H. Zhao, Appl. Phys. Lett. 115, 120602 (2019).

40. . R. Wakabayashi, K. Yoshimatsu, M. Hattori, J.-S. Lee, O. Sakata, A. Ohtomo, Cryst. Growth Des.21, 2844 (2021).

41. S.W. Kaun, F. Wu, and J.S. Speck, J. Vac. Sci. Technol., A 33, 041508 (2015).

42. R. Miller, F. Alema, and A. Osinsky, IEEE Trans. Semicond. Manuf. 31, 467 (2018).

43. A.F.M.A.U. Bhuiyan, Z. Feng, J.M. Johnson, H.L. Huang, J. Sarker, M. Zhu, M.R. Karim, B. Mazumder, J. Hwang and H. Zhao. APL Mater. 8, 031104 (2020).

44. J. Sarker, S. Broderick, A.F.M.A.U. Bhuiyan, Z. Feng, H. Zhao and B. Mazumder, Appl. Phys. Lett. 116, 152101 (2020).

45. H. Peelaers, J.B. Varley, J.S. Speck, C.G. Van de Walle, Appl.Phys. Lett. 112, 242101 (2018).

46. H. Kim, H. Ko, Y.-C. Chung, S.B. Cho, J. Eur. Ceram. Soc. 41, 611 (2020).

47. T. Wang, W. Li, C. Ni, A. Janotti, Phys. Rev. Appl. 10, 011003 (2018).

48. M. Hilfiker, U. Kilic, A. Mock, V. Darakchieva, S. Knight, R. Korlacki, A. Mauze, Y. Zhang, J. Speck, M. Schubert, Appl. Phys.Lett. 114, 231901 (2019).

49. H. von Wenckstern, M. Kneiß, A. Hassa, P. Storm, D. Splith and M. Grundmann, Physica Status Solidi (B) Basic Research, 1900626, 1 (2019).

50. H. von Wenckstern, Z. Zhang, F. Schmidt, J. Lenzner, H. Hochmuth and M. Grundmann, Cryst Eng Comm, 15, 10020 (2013).

51. Chaker Fares, Zahabul Islam, Aman Haque, Max Kneiß, Holger von Wenckstern, Marius Grundmann, Marko Tadjer, Fan Ren and S.J. Pearton, ECS J. Solid State Sci. Technol.8, P751 (2019).

52. Chaker Fares, Max Kneiß , Holger von Wenckstern, Marko Tadjer, Fan Ren, Eric Lambers, Marius Grundmann and S.J. Pearton, ECS J. Solid State Sci. Technol.8, Q P351 (2019).

53. David C. Hays, B. P. Gila, S. J. Pearton, and F. Ren, Appl. Phys. Rev. 4, 021301 (2017).

54. J. B. Varley, J. Mater. Res. (in press, 2021)

Table 1. Summary of the measured reference and heterostructure peaks for SiO_2 on $(Al_xGa_{1-x})_2O_3$ (eV)

	Reference $(Al_xGa_{1-x})_2O_3$			Reference SiO_2			Thin SiO_2 on $(Al_xGa_{1-x})_2O_3$	
Aluminum Concentration	Core Level Peak (Ga $2p_{3/2}$)	VBM	Core - VBM	Core Level Peak (Si 2p)	VBM	Core - VBM	Δ Core Level (Ga $2p_{3/2}$- Si 2p)	Valence Band Offset
$(Al_{0.26}Ga_{0.74})_2O_3$	1117.7	2.7±0.15	1115	103.40	4.80	98.60	1017.6	-1.2
$(Al_{0.42}Ga_{0.58})_2O_3$	1118.2	3.3±0.15	1114.9	-	-	-	1016.5	-0.2
$(Al_{0.58}Ga_{0.42})_2O_3$	1119.2	4.4±0.15	1114.7	-	-	-	1015.9	0.2
$(Al_{0.74}Ga_{0.26})_2O_3$	1118.9	4.5±0.15	1114.5	-	-	-	1015.5	0.4

Figure Captions

Figure 1. Crystal structure of rhombohedral α -Ga_2O_3. The oxygen atoms are displayed as red and the Ga atoms as green spheres. The graphic was created with the software Crystal Maker X, http://www.crystalmaker.com/about/index.html .

Figure 2. (a) Al content x at 49 points across the thin film surface, marked on the map as black dots and determined by EDX. The data between the measurement points was interpolated, the black arrow represents the direction of the gradient. (b) Al ratio x acquired along the indicated gradient in (a) by EDX and XPS, respectively.

Figure 3. False color map of θ-ω scans of α-$(Al_xGa_{1-x})_2O_3$ recorded along the composition gradient indicated in Figure 2(b).

Figure 4. XPS spectra of core levels to valence band maximum (VBM) for reference $(Al_xGa_{1-x})_2O_3$ with x= 0.26, 0.42, 0.58 or 0.74 (top to bottom) Aluminum, and (c) ALD thick film Al_2O_3 and SiO_2.The intensity is in arbitrary units (a.u.).

Figure 5. XPS spectra of core levels to valence band maximum (VBM) for ALD thick film SiO_2.The intensity is in arbitrary units (a.u.).

Figure 6. Bandgap of α-$(Al_xGa_{1-x})_2O_3$ determined using the onset of the plasmon loss feature in O 1s photoemission spectrum. The intensities are in arbitrary units (a.u.).

Figure 7. Bandgap of α-$(Al_xGa_{1-x})_2O_3$ for 4 Al compositions (experimental points) fitted to a bowing parameter of 3eV, along with a theoretical curve with bowing parameter 1.37 eV.

Figure 8. Band diagrams for the SiO_2/α-$(Al_xGa_{1-x})_2O_3$ heterostructure in which the SiO_2 was deposited by ALD.

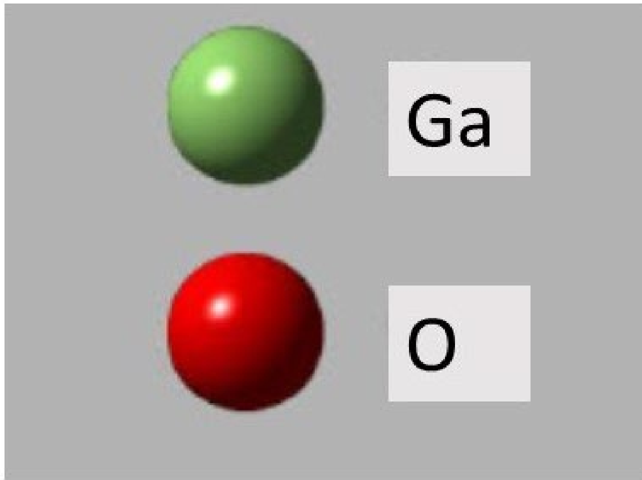
Ga
O

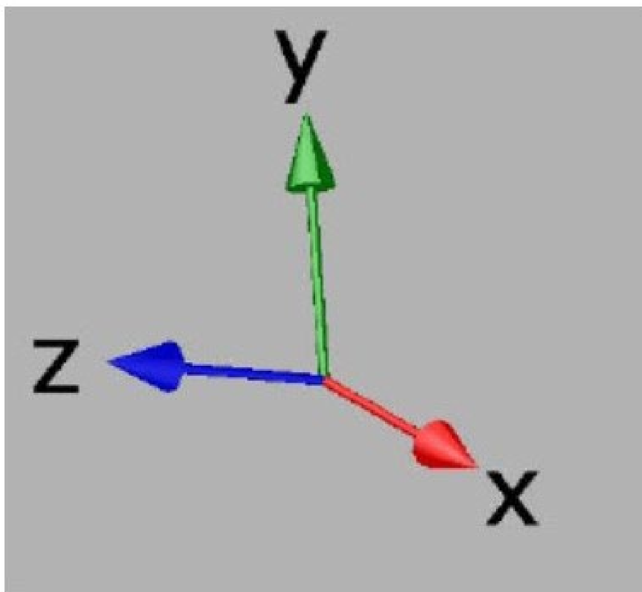
y
z
x

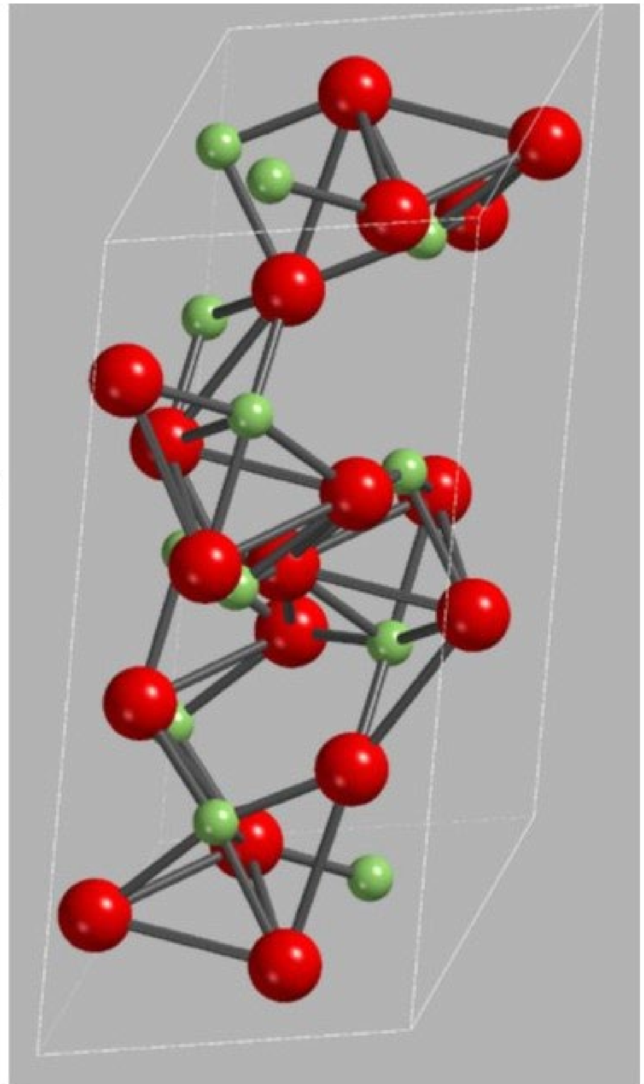

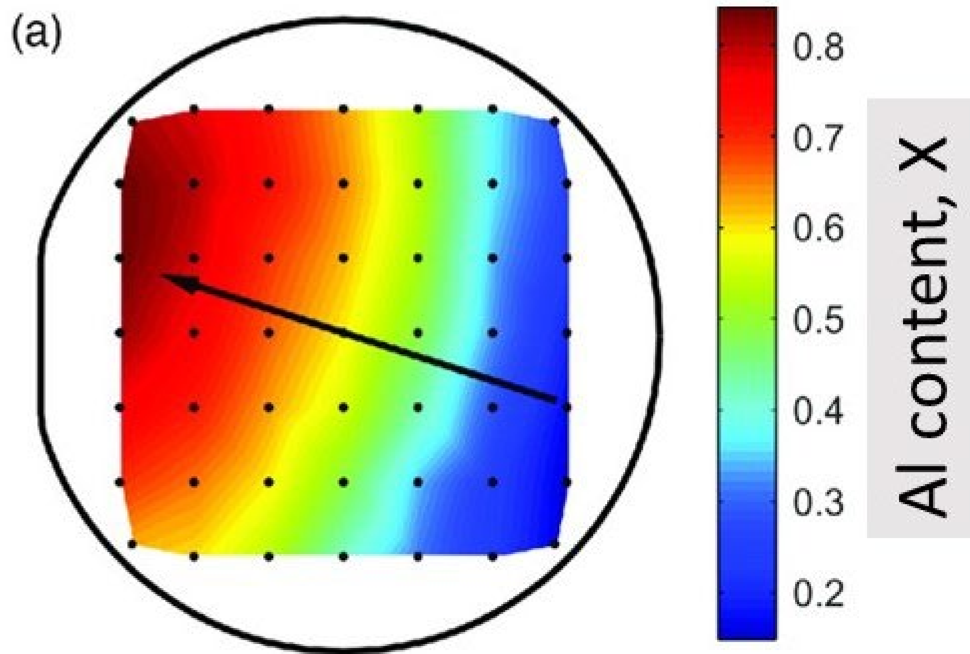
(a)
0.8
0.7
0.6
0.5
0.4
0.3
0.2
Al content, X

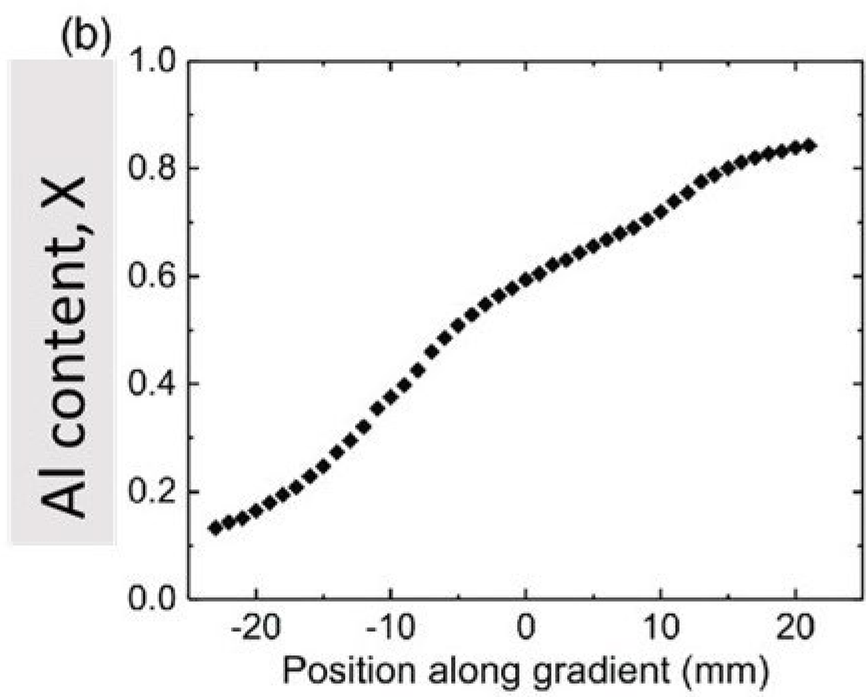
(b)
Al content, X
1.0
0.8
0.6
0.4
0.2
0.0
-20
-10
0
10
20
Position along gradient (mm)

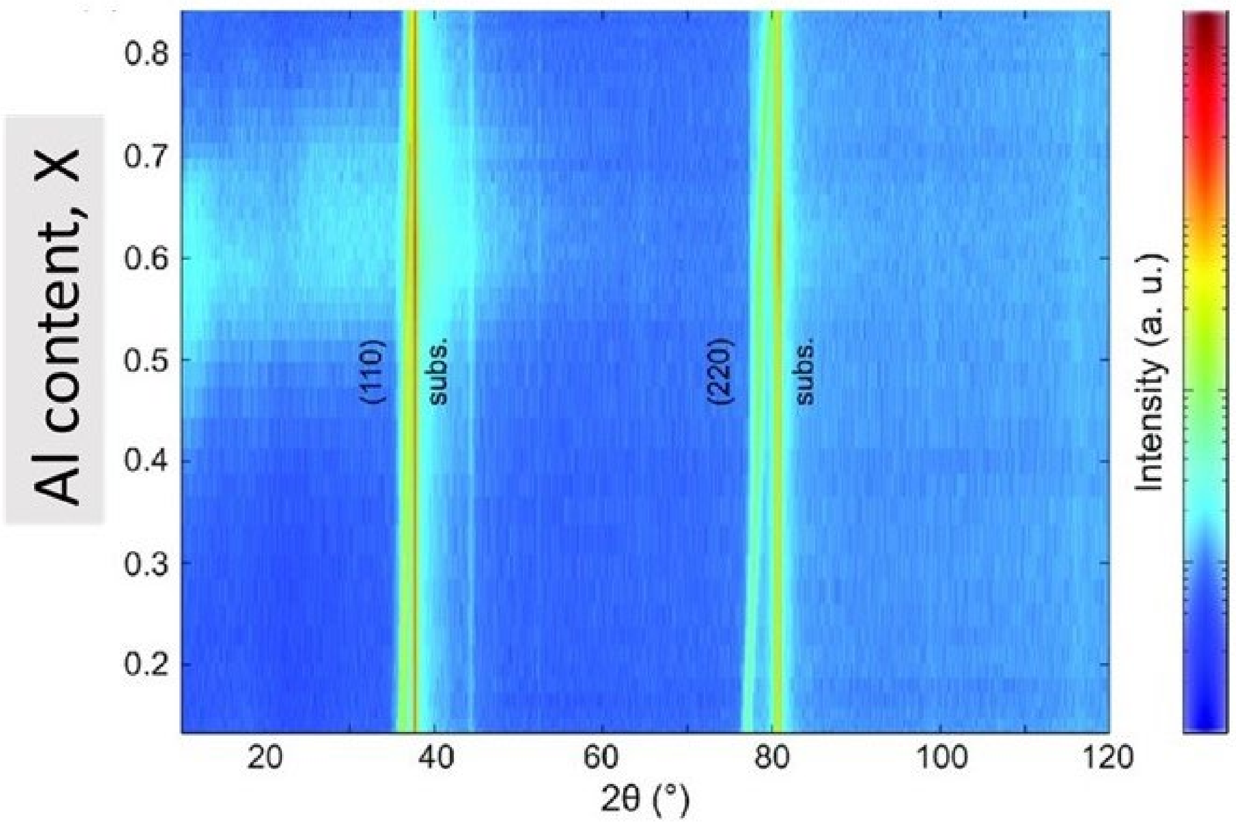
Al content, X
0.8
0.7
0.6
0.5
0.4
0.3
0.2
(110)
subs.
(220)
subs.
20
40
60
80
100
120
2θ (°)
Intensity (a. u.)

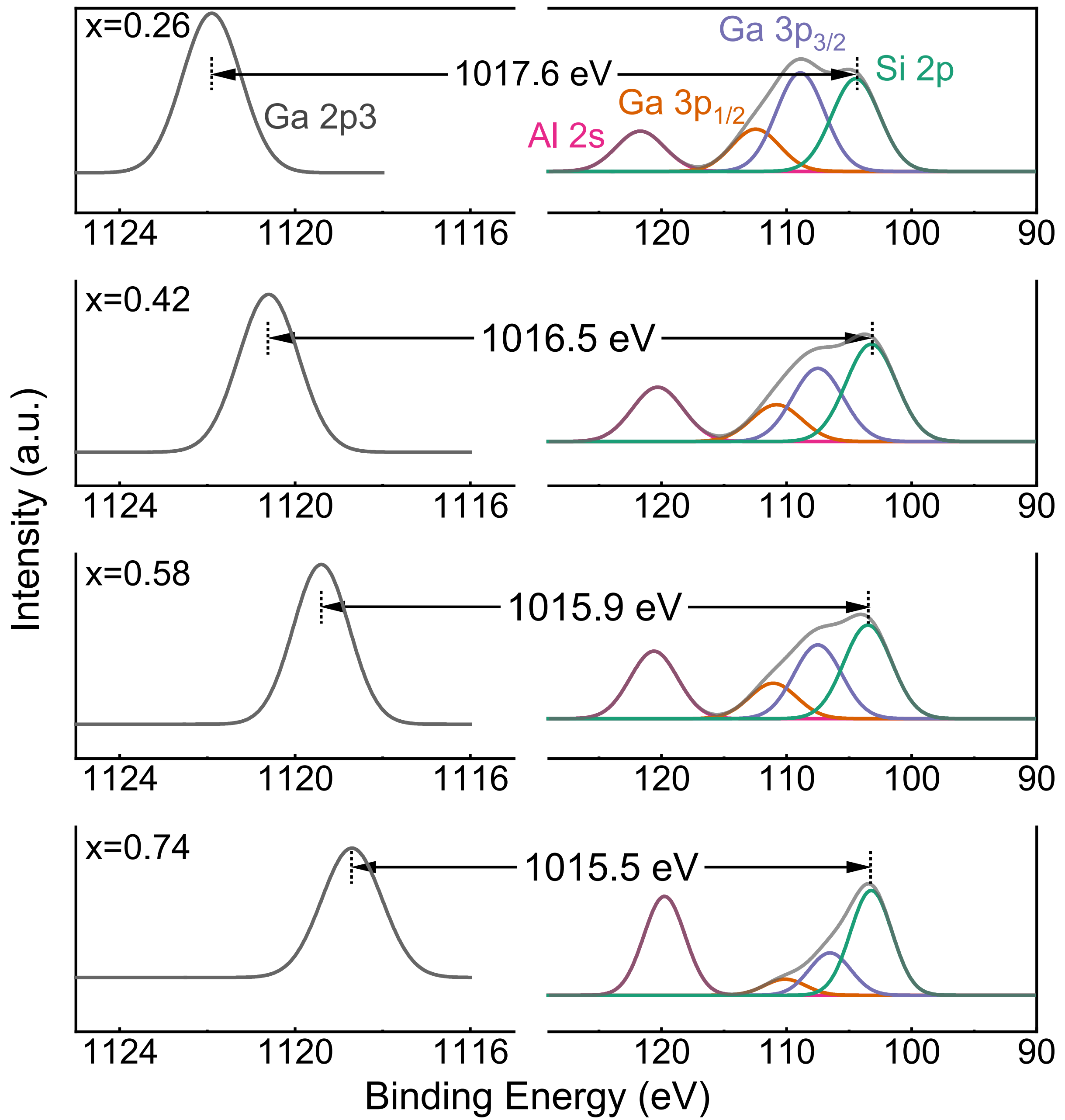
SiO2 on (AlxGa1-x)2O3
x=0.26
Ga 2p3
1017.6 eV
Ga 3p3/2
Si 2p
Ga 3p1/2
Al 2s
x=0.42
1016.5 eV
x=0.58
1015.9 eV
x=0.74
1015.5 eV
1124
1120
1116
120
110
100
90
Intensity (a.u.)
Binding Energy (eV)

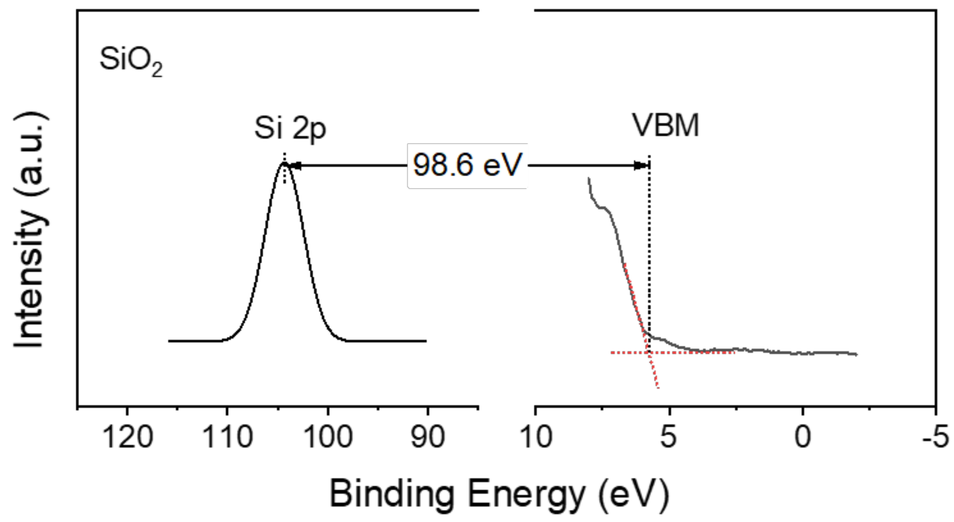
SiO2
Si 2p
98.6 eV
VBM
Intensity (a.u.)
120
110
100
90
10
5
0
-5
Binding Energy (eV)

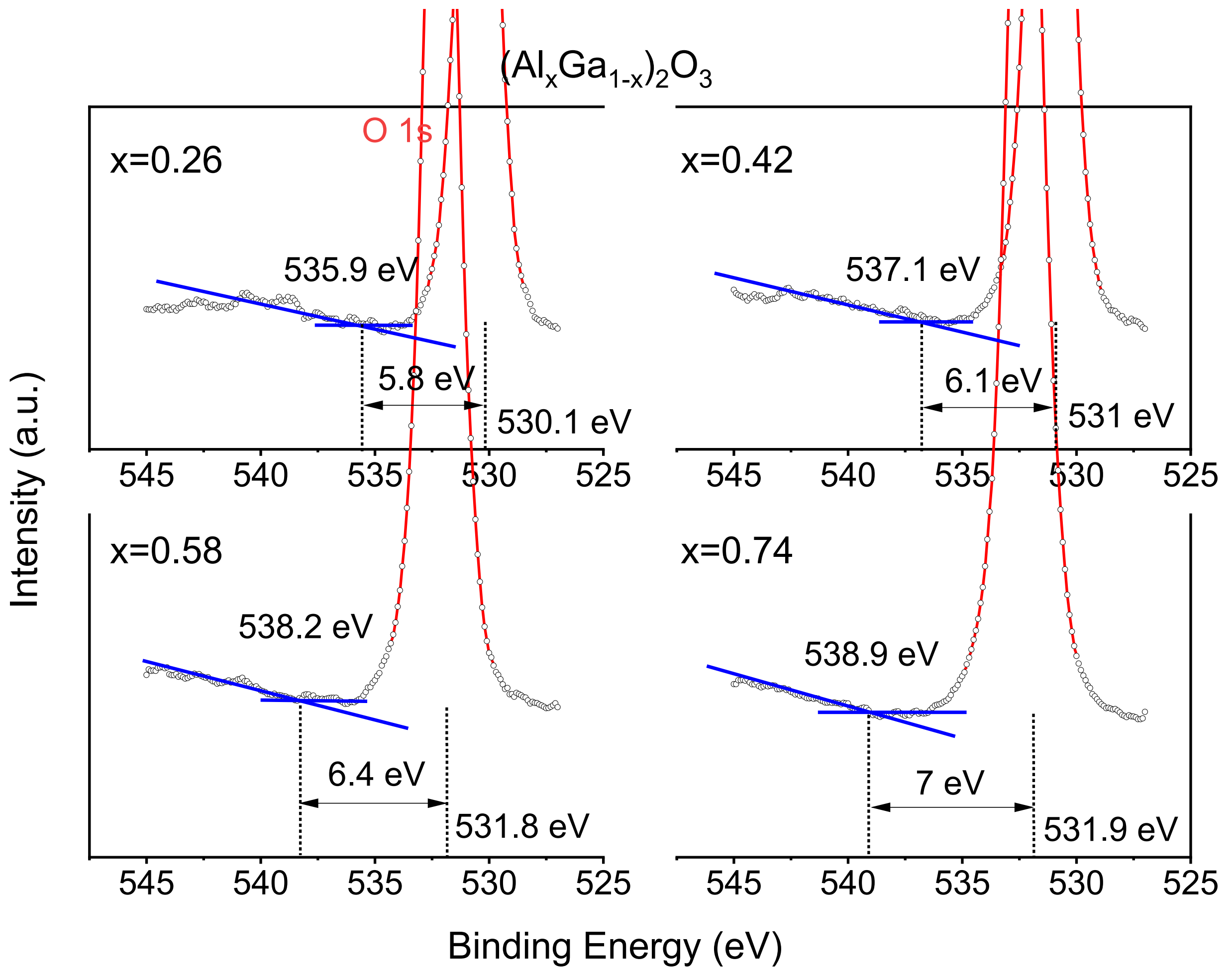

(Al$_x$Ga$_{1-x}$)$_2$O$_3$
O 1s
x=0.26
535.9 eV
5.8 eV
530.1 eV
x=0.42
537.1 eV
6.1 eV
531 eV
x=0.58
538.2 eV
6.4 eV
531.8 eV
x=0.74
538.9 eV
7 eV
531.9 eV
545
540
535
530
525
Intensity (a.u.)
Binding Energy (eV)

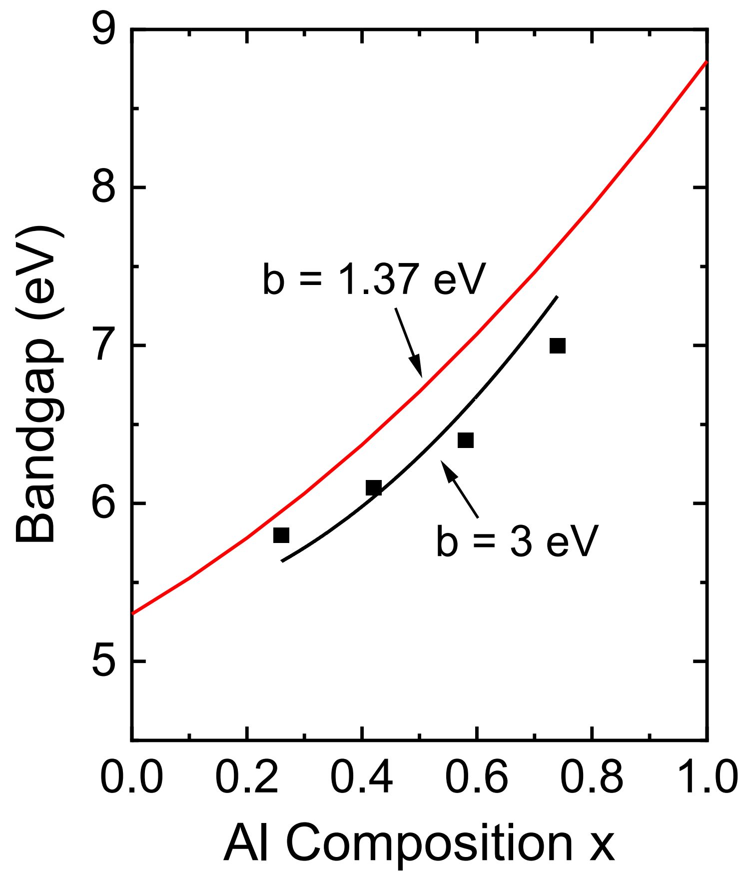
9
8
7
6
5
Bandgap (eV)
b = 1.37 eV
b = 3 eV
0.0
0.2
0.4
0.6
0.8
1.0
Al Composition x

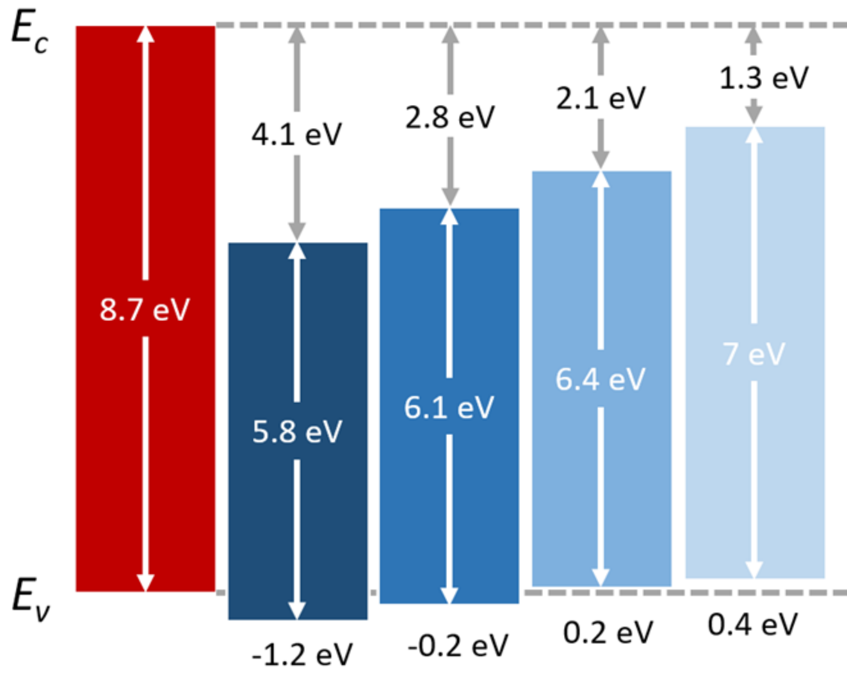
SiO2
(AlxGa1-x)2O3
x=0.26
x=0.42
x=0.58
x=0.74
Ec
Ev
8.7 eV
4.1 eV
5.8 eV
2.8 eV
6.1 eV
2.1 eV
6.4 eV
1.3 eV
7 eV
-1.2 eV
-0.2 eV
0.2 eV
0.4 eV